A search for gravitational waves associated with the August 2006 timing glitch of the Vela pulsar

J. Abadie,[17] B. P. Abbott,[17] R. Abbott,[17] R. Adhikari,[17] P. Ajith,[17] B. Allen,[2, 60] G. Allen,[35] E. Amador Ceron,[60] R. S. Amin,[21] S. B. Anderson,[17] W. G. Anderson,[60] M. A. Arain,[47] M. Araya,[17] Y. Aso,[17] S. Aston,[46] P. Aufmuth,[16] C. Aulbert,[2] S. Babak,[1] P. Baker,[24] S. Ballmer,[17] D. Barker,[18] B. Barr,[48] P. Barriga,[59] L. Barsotti,[20] M. A. Barton,[18] I. Bartos,[10] R. Bassiri,[48] M. Bastarrika,[48] B. Behnke,[1] M. Benacquista,[42] M. F. Bennett,[38] J. Betzwieser,[17] P. T. Beyersdorf,[31] I. A. Bilenko,[25] G. Billingsley,[17] R. Biswas,[60] E. Black,[17] J. K. Blackburn,[17] L. Blackburn,[20] D. Blair,[59] B. Bland,[18] O. Bock,[2] T. P. Bodiya,[20] R. Bondarescu,[37] R. Bork,[17] M. Born,[2] S. Bose,[61] P. R. Brady,[60] V. B. Braginsky,[25] J. E. Brau,[53] J. Breyer,[2] D. O. Bridges,[19] M. Brinkmann,[2] M. Britzger,[2] A. F. Brooks,[17] D. A. Brown,[36] A. Bullington,[35] A. Buonanno,[49] O. Burmeister,[2] R. L. Byer,[35] L. Cadonati,[50] J. Cain,[39] J. B. Camp,[26] J. Cannizzo,[26] K. C. Cannon,[17] J. Cao,[20] C. Capano,[36] L. Cardenas,[17] S. Caudill,[21] M. Cavaglià,[39] C. Cepeda,[17] T. Chalermsongsak,[17] E. Chalkley,[48] P. Charlton,[9] S. Chatterji,[17] S. Chelkowski,[46] Y. Chen,[6] N. Christensen,[8] S. S. Y. Chua,[4] C. T. Y. Chung,[38] D. Clark,[35] J. Clark,[7] J. H. Clayton,[60] R. Conte,[55] D. Cook,[18] T. R. C. Corbitt,[20] N. Cornish,[24] D. Coward,[59] D. C. Coyne,[17] J. D. E. Creighton,[60] T. D. Creighton,[42] A. M. Cruise,[46] R. M. Culter,[46] A. Cumming,[48] L. Cunningham,[48] K. Dahl,[2] S. L. Danilishin,[25] K. Danzmann,[2, 16] B. Daudert,[17] G. Davies,[7] E. J. Daw,[40] T. Dayanga,[61] D. DeBra,[35] J. Degallaix,[2] V. Dergachev,[51] R. DeSalvo,[17] S. Dhurandhar,[15] M. Díaz,[42] F. Donovan,[20] K. L. Dooley,[47] E. E. Doomes,[34] R. W. P. Drever,[5] J. Driggers,[17] J. Dueck,[2] I. Duke,[20] J. -C. Dumas,[59] M. Edgar,[48] M. Edwards,[7] A. Effler,[18] P. Ehrens,[17] T. Etzel,[17] M. Evans,[20] T. Evans,[19] S. Fairhurst,[7] Y. Faltas,[47] Y. Fan,[59] D. Fazi,[17] H. Fehrmann,[2] L. S. Finn,[37] K. Flasch,[60] S. Foley,[20] C. Forrest,[54] N. Fotopoulos,[60] M. Frede,[2] M. Frei,[41] Z. Frei,[12] A. Freise,[46] R. Frey,[53] T. T. Fricke,[21] D. Friedrich,[2] P. Fritschel,[20] V. V. Frolov,[19] P. Fulda,[46] M. Fyffe,[19] J. A. Garofoli,[36] S. Ghosh,[61] J. A. Giaime,[21, 19] S. Giampanis,[2] K. D. Giardina,[19] E. Goetz,[51] L. M. Goggin,[60] G. González,[21] S. Goßler,[2] A. Grant,[48] S. Gras,[59] C. Gray,[18] R. J. S. Greenhalgh,[30] A. M. Gretarsson,[11] R. Grosso,[42] H. Grote,[2] S. Grunewald,[1] E. K. Gustafson,[17] R. Gustafson,[51] B. Hage,[16] J. M. Hallam,[46] D. Hammer,[60] G. D. Hammond,[48] C. Hanna,[17] J. Hanson,[19] J. Harms,[52] G. M. Harry,[20] I. W. Harry,[7] E. D. Harstad,[53] K. Haughian,[48] K. Hayama,[2] T. Hayler,[30] J. Heefner,[17] I. S. Heng,[48] A. Heptonstall,[17] M. Hewitson,[2] S. Hild,[46] E. Hirose,[36] D. Hoak,[19] K. A. Hodge,[17] K. Holt,[19] D. J. Hosken,[45] J. Hough,[48] E. Howell,[59] D. Hoyland,[46] B. Hughey,[20] S. Husa,[44] S. H. Huttner,[48] D. R. Ingram,[18] T. Isogai,[8] A. Ivanov,[17] W. W. Johnson,[21] D. I. Jones,[57] G. Jones,[7] R. Jones,[48] L. Ju,[59] P. Kalmus,[17] V. Kalogera,[28] S. Kandhasamy,[52] J. Kanner,[49] E. Katsavounidis,[20] K. Kawabe,[18] S. Kawamura,[27] F. Kawazoe,[2] W. Kells,[17] D. G. Keppel,[17] A. Khalaidovski,[2] F. Y. Khalili,[25] R. Khan,[10] E. Khazanov,[14] H. Kim,[2] P. J. King,[17] J. S. Kissel,[21] S. Klimenko,[47] K. Kokeyama,[27] V. Kondrashov,[17] R. Kopparapu,[37] S. Koranda,[60] D. Kozak,[17] V. Kringel,[2] B. Krishnan,[1] G. Kuehn,[2] J. Kullman,[2] R. Kumar,[48] P. Kwee,[16] P. K. Lam,[4] M. Landry,[18] M. Lang,[37] B. Lantz,[35] N. Lastzka,[2] A. Lazzarini,[17] P. Leaci,[2] M. Lei,[17] N. Leindecker,[35] I. Leonor,[53] H. Lin,[47] P. E. Lindquist,[17] T. B. Littenberg,[24] N. A. Lockerbie,[58] D. Lodhia,[46] M. Lormand,[19] P. Lu,[35] M. Lubinski,[18] A. Lucianetti,[47] H. Lück,[2, 16] A. Lundgren,[36] B. Machenschalk,[2] M. MacInnis,[20] M. Mageswaran,[17] K. Mailand,[17] C. Mak,[17] I. Mandel,[28] V. Mandic,[52] S. Márka,[10] Z. Márka,[10] A. Markosyan,[35] J. Markowitz,[20] E. Maros,[17] I. W. Martin,[48] R. M. Martin,[47] J. N. Marx,[17] K. Mason,[20] F. Matichard,[20, 21] L. Matone,[10] R. A. Matzner,[41] N. Mavalvala,[20] R. McCarthy,[18] D. E. McClelland,[4] S. C. McGuire,[34] G. McIntyre,[17] D. J. A. McKechan,[7] M. Mehmet,[2] A. Melatos,[38] A. C. Melissinos,[54] G. Mendell,[18] D. F. Menéndez,[37] R. A. Mercer,[60] L. Merrill,[59] S. Meshkov,[17] C. Messenger,[2] M. S. Meyer,[19] H. Miao,[59] J. Miller,[48] Y. Mino,[6] S. Mitra,[17] V. P. Mitrofanov,[25] G. Mitselmakher,[47] R. Mittleman,[20] O. Miyakawa,[17] B. Moe,[60] S. D. Mohanty,[42] S. R. P. Mohapatra,[50] G. Moreno,[18] K. Mors,[2] K. Mossavi,[2] C. MowLowry,[4] G. Mueller,[47] H. Müller-Ebhardt,[2] S. Mukherjee,[42] A. Mullavey,[4] J. Munch,[45] P. G. Murray,[48] T. Nash,[17] R. Nawrodt,[48] J. Nelson,[48] G. Newton,[48] E. Nishida,[27] A. Nishizawa,[27] J. O'Dell,[30] B. O'Reilly,[19] R. O'Shaughnessy,[37] E. Ochsner,[49] G. H. Ogin,[17] R. Oldenburg,[60] D. J. Ottaway,[45] R. S. Ottens,[47] H. Overmier,[19] B. J. Owen,[37] A. Page,[46] Y. Pan,[49] C. Pankow,[47] M. A. Papa,[1, 60] P. Patel,[17] D. Pathak,[7] M. Pedraza,[17] L. Pekowsky,[36] S. Penn,[13] C. Peralta,[1] A. Perreca,[46] M. Pickenpack,[2] I. M. Pinto,[56] M. Pitkin,[48] H. J. Pletsch,[2] M. V. Plissi,[48] F. Postiglione,[56] M. Principe,[56] R. Prix,[2] L. Prokhorov,[25] O. Puncken,[2] V. Quetschke,[42] F. J. Raab,[18] D. S. Rabeling,[4] H. Radkins,[18] P. Raffai,[12] Z. Raics,[10] M. Rakhmanov,[42] V. Raymond,[28] C. M. Reed,[18] T. Reed,[22] H. Rehbein,[2] S. Reid,[48] D. H. Reitze,[47] R. Riesen,[19] K. Riles,[51] P. Roberts,[3] N. A. Robertson,[17, 48] C. Robinson,[7] E. L. Robinson,[1] S. Roddy,[19] C. Röver,[2] J. Rollins,[10] J. D. Romano,[42] J. H. Romie,[19] S. Rowan,[48] A. Rüdiger,[2] K. Ryan,[18] S. Sakata,[27] L. Sammut,[38] L. Sancho de la Jordana,[44] V. Sandberg,[18] V. Sannibale,[17] L. Santamaría,[1] G. Santostasi,[23]

S. Saraf,[32] P. Sarin,[20] B. S. Sathyaprakash,[7] S. Sato,[27] M. Satterthwaite,[4] P. R. Saulson,[36] R. Savage,[18]
R. Schilling,[2] R. Schnabel,[2] R. Schofield,[53] B. Schulz,[2] B. F. Schutz,[1, 7] P. Schwinberg,[18] J. Scott,[48] S. M. Scott,[4]
A. C. Searle,[17] F. Seifert,[2, 17] D. Sellers,[19] A. S. Sengupta,[17] A. Sergeev,[14] B. Shapiro,[20] P. Shawhan,[49]
D. H. Shoemaker,[20] A. Sibley,[19] X. Siemens,[60] D. Sigg,[18] A. M. Sintes,[44] G. Skelton,[60] B. J. J. Slagmolen,[4]
J. Slutsky,[21] J. R. Smith,[36] M. R. Smith,[17] N. D. Smith,[20] K. Somiya,[6] B. Sorazu,[48] F. Speirits,[48] A. J. Stein,[20]
L. C. Stein,[20] S. Steplewski,[61] A. Stochino,[17] R. Stone,[42] K. A. Strain,[48] S. Strigin,[25] A. Stroeer,[26] A. L. Stuver,[19]
T. Z. Summerscales,[3] M. Sung,[21] S. Susmithan,[59] P. J. Sutton,[7] G. P. Szokoly,[12] D. Talukder,[61] D. B. Tanner,[47]
S. P. Tarabrin,[25] J. R. Taylor,[2] R. Taylor,[17] K. A. Thorne,[19] K. S. Thorne,[6] A. Thüring,[16] C. Titsler,[37]
K. V. Tokmakov,[48, 58] C. Torres,[19] C. I. Torrie,[17, 48] G. Traylor,[19] M. Trias,[44] L. Turner,[17] D. Ugolini,[43]
K. Urbanek,[35] H. Vahlbruch,[16] M. Vallisneri,[6] C. Van Den Broeck,[7] M. V. van der Sluys,[28] A. A. van Veggel,[48]
S. Vass,[17] R. Vaulin,[60] A. Vecchio,[46] J. Veitch,[46] P. J. Veitch,[45] C. Veltkamp,[2] A. Villar,[17] C. Vorvick,[18]
S. P. Vyachanin,[25] S. J. Waldman,[20] L. Wallace,[17] A. Wanner,[2] R. L. Ward,[17] P. Wei,[36] M. Weinert,[2]
A. J. Weinstein,[17] R. Weiss,[20] L. Wen,[59, 6] S. Wen,[21] P. Wessels,[2] M. West,[36] T. Westphal,[2] K. Wette,[4]
J. T. Whelan,[29] S. E. Whitcomb,[17] B. F. Whiting,[47] C. Wilkinson,[18] P. A. Willems,[17] H. R. Williams,[37]
L. Williams,[47] B. Willke,[2, 16] I. Wilmut,[30] L. Winkelmann,[2] W. Winkler,[2] C. C. Wipf,[20] A. G. Wiseman,[60]
G. Woan,[48] R. Wooley,[19] J. Worden,[18] I. Yakushin,[19] H. Yamamoto,[17] K. Yamamoto,[2] D. Yeaton-Massey,[17]
S. Yoshida,[33] M. Zanolin,[11] L. Zhang,[17] Z. Zhang,[59] C. Zhao,[59] N. Zotov,[22] M. E. Zucker,[20] and J. Zweizig[17]
(The LIGO Scientific Collaboration, http://www.ligo.org)

S. Buchner[62]

[1] Albert-Einstein-Institut, Max-Planck-Institut für Gravitationsphysik, D-14476 Golm, Germany
[2] Albert-Einstein-Institut, Max-Planck-Institut für Gravitationsphysik, D-30167 Hannover, Germany
[3] Andrews University, Berrien Springs, MI 49104 USA
[4] Australian National University, Canberra, 0200, Australia
[5] California Institute of Technology, Pasadena, CA 91125, USA
[6] Caltech-CaRT, Pasadena, CA 91125, USA
[7] Cardiff University, Cardiff, CF24 3AA, United Kingdom
[8] Carleton College, Northfield, MN 55057, USA
[9] Charles Sturt University, Wagga Wagga, NSW 2678, Australia
[10] Columbia University, New York, NY 10027, USA
[11] Embry-Riddle Aeronautical University, Prescott, AZ 86301 USA
[12] Eötvös University, ELTE 1053 Budapest, Hungary
[13] Hobart and William Smith Colleges, Geneva, NY 14456, USA
[14] Institute of Applied Physics, Nizhny Novgorod, 603950, Russia
[15] Inter-University Centre for Astronomy and Astrophysics, Pune - 411007, India
[16] Leibniz Universität Hannover, D-30167 Hannover, Germany
[17] LIGO - California Institute of Technology, Pasadena, CA 91125, USA
[18] LIGO - Hanford Observatory, Richland, WA 99352, USA
[19] LIGO - Livingston Observatory, Livingston, LA 70754, USA
[20] LIGO - Massachusetts Institute of Technology, Cambridge, MA 02139, USA
[21] Louisiana State University, Baton Rouge, LA 70803, USA
[22] Louisiana Tech University, Ruston, LA 71272, USA
[23] McNeese State University, Lake Charles, LA 70609, USA
[24] Montana State University, Bozeman, MT 59717, USA
[25] Moscow State University, Moscow, 119992, Russia
[26] NASA/Goddard Space Flight Center, Greenbelt, MD 20771, USA
[27] National Astronomical Observatory of Japan, Tokyo 181-8588, Japan
[28] Northwestern University, Evanston, IL 60208, USA
[29] Rochester Institute of Technology, Rochester, NY 14623, USA
[30] Rutherford Appleton Laboratory, HSIC, Chilton, Didcot, Oxon OX11 0QX United Kingdom
[31] San Jose State University, San Jose, CA 95192, USA
[32] Sonoma State University, Rohnert Park, CA 94928, USA
[33] Southeastern Louisiana University, Hammond, LA 70402, USA
[34] Southern University and A&M College, Baton Rouge, LA 70813, USA
[35] Stanford University, Stanford, CA 94305, USA
[36] Syracuse University, Syracuse, NY 13244, USA
[37] The Pennsylvania State University, University Park, PA 16802, USA
[38] The University of Melbourne, Parkville VIC 3010, Australia
[39] The University of Mississippi, University, MS 38677, USA
[40] The University of Sheffield, Sheffield S10 2TN, United Kingdom

^{41} *The University of Texas at Austin, Austin, TX 78712, USA*
^{42} *The University of Texas at Brownsville and Texas Southmost College, Brownsville, TX 78520, USA*
^{43} *Trinity University, San Antonio, TX 78212, USA*
^{44} *Universitat de les Illes Balears, E-07122 Palma de Mallorca, Spain*
^{45} *University of Adelaide, Adelaide, SA 5005, Australia*
^{46} *University of Birmingham, Birmingham, B15 2TT, United Kingdom*
^{47} *University of Florida, Gainesville, FL 32611, USA*
^{48} *University of Glasgow, Glasgow, G12 8QQ, United Kingdom*
^{49} *University of Maryland, College Park, MD 20742 USA*
^{50} *University of Massachusetts - Amherst, Amherst, MA 01003, USA*
^{51} *University of Michigan, Ann Arbor, MI 48109, USA*
^{52} *University of Minnesota, Minneapolis, MN 55455, USA*
^{53} *University of Oregon, Eugene, OR 97403, USA*
^{54} *University of Rochester, Rochester, NY 14627, USA*
^{55} *University of Salerno, I-84084 Fisciano (Salerno), Italy and INFN*
^{56} *University of Sannio at Benevento, I-82100 Benevento, Italy and INFN*
^{57} *University of Southampton, Southampton, SO17 1BJ, United Kingdom*
^{58} *University of Strathclyde, Glasgow, G1 1XQ, United Kingdom*
^{59} *University of Western Australia, Crawley, WA 6009, Australia*
^{60} *University of Wisconsin-Milwaukee, Milwaukee, WI 53201, USA*
^{61} *Washington State University, Pullman, WA 99164, USA*
^{62} *HartRAO, Krugersdorp, South Africa*
(Dated: November 8, 2010)

The physical mechanisms responsible for pulsar timing glitches are thought to excite quasi-normal mode oscillations in their parent neutron star that couple to gravitational wave emission. In August 2006, a timing glitch was observed in the radio emission of PSR B0833−45, the Vela pulsar. At the time of the glitch, the two co-located Hanford gravitational wave detectors of the Laser Interferometer Gravitational-wave observatory (LIGO) were operational and taking data as part of the fifth LIGO science run (S5). We present the first direct search for the gravitational wave emission associated with oscillations of the fundamental quadrupole mode excited by a pulsar timing glitch. No gravitational wave detection candidate was found. We place Bayesian 90% confidence upper limits of 6.3×10^{-21} to 1.4×10^{-20} on the peak intrinsic strain amplitude of gravitational wave ring-down signals, depending on which spherical harmonic mode is excited. The corresponding range of energy upper limits is 5.0×10^{44} to 1.3×10^{45} erg.

PACS numbers: 04.80.Nn, 07.05.Kf, 95.85.Sz, 97.60.Gb

I. INTRODUCTION

Neutron stars are often regarded as a prime source of various forms of gravitational wave emission. Recent searches for gravitational wave emission from neutron star systems include the search for the continuous, near-monochromatic emission from rapidly rotating deformed neutron stars [1] and the characteristic chirp signal associated with the coalescence of a binary neutron star or neutron star-black hole system [2, 3]. An additional mechanism for the radiation of gravitational waves from neutron stars is the excitation of quasi-normal modes (QNMs) (see, for example, [4–11] and the references therein). This excitation could occur as a consequence of flaring activity in soft-gamma repeaters [12–14], the formation of a hyper-massive neutron star following the coalescence of a binary neutron star system [15], or be associated with a pulsar timing glitch caused by a starquake or transfer of angular momentum from a superfluid core to a solid crust [16, 17].

In this paper, we report the results of a search in data from the fifth science run (S5) of the Laser Interferometer Gravitational-wave Observatory (LIGO) for a gravitational wave signal produced by QNM excitation associated with a timing glitch in the Vela pulsar in August 2006. In Sec. II, we briefly describe the radio observations of the timing glitch that motivates this search and the status of the LIGO gravitational wave detectors. In Sec. III, we describe the phenomenon of pulsar glitches and the expected gravitational wave emission. Section IV describes the details of the signal we search for and the Bayesian model selection algorithm used for the analysis. Section V reports the results of the gravitational wave search. Characterization of the sensitivity of the search is described in Sec. VI. In Sec. VII, we discuss these results and the prospects for future searches.

II. A GLITCH IN PSR B0833−45

A. Electromagnetic observations

PSR B0833−45, known colloquially as the Vela pulsar, is monitored almost daily by the Hartebeesthoek radio observatory (HartRAO) in South Africa. HartRAO performed three observations per day at 1668 MHz and

2272 MHz using a 26 m telescope in a monitoring program that ran from 1985 to 2008 [18]. The radio pulse arrival times collected by HartRAO indicate that a sudden increase in rotational frequency, a phenomenon known as a pulsar glitch, occurred on August 12$^{\text{th}}$ 2006.

Following [19], observations of pulse arrival times from a pulsar can be converted to rotational (angular) frequency residuals $\Delta\Omega$ relative to a simple pre-glitch spin-down model of the form

$$\Omega(t) = \Omega_0 + \dot{\Omega}t, \qquad (1)$$

where Ω_0 is the spin frequency at some reference time t_0 and $\dot{\Omega}$ is its time derivative. The post-glitch evolution of these frequency residuals can be described as a permanent change in rotational frequency $\Delta\Omega_p$ and its first and second derivatives $\Delta\dot{\Omega}_p$ and $\Delta\ddot{\Omega}_p$, plus one or more transient components which decay exponentially on a time-scale τ_i and have amplitude $\Delta\Omega_i$. At time t, the residuals between the frequency of pulses expected from the model in Eq. (1) and those which are observed following a glitch are then,

$$\Delta\Omega(t) = \Delta\Omega_p + \Delta\dot{\Omega}_p t + \frac{1}{2}\Delta\ddot{\Omega}_p t^2 + \sum_{i=1}^{N}\Delta\Omega_i e^{-t/\tau_i}, \quad (2)$$

For this analysis we determined the glitch epoch by splitting the HartRAO observations into pre- and post-glitch data sets. Equation (1) was used to model 10 days of pre-glitch data. Shorter lengths of post-glitch data (2, 3 and 4 days) were then used to determine appropriate post-glitch decay time-scales in Eq. (2) for this event. This yields a model for the post-glitch frequency residual evolution. These pre- and post-glitch models were then fitted to the HartRAO data using the TEMPO2 phase-fitting software [20]. The intersection of these models then determines the glitch epoch.

We find that the glitch epoch is MJD 53959.9392 ± 0.0002 in terms of barycentric dynamical time at the solar system barycenter (UTC 2006–08–12 22:31:22 ±17, at the center of the Earth). The analysis presented in this work assumes the gravitational wave emission is co-incident in time with the reported glitch epoch and uses 120 seconds of data centered on the glitch epoch corresponding to a timing uncertainty of greater than 3-σ.

The magnitude of the glitch, relative to the pre-glitch rotational frequency of $\Omega_0 \approx 2\pi \times 11 \text{ rads}^{-1}$, was $\Delta\Omega/\Omega_0 = 2.620 \times 10^{-6}$ [21]. For comparison, the largest glitch observed to date in the Vela pulsar had magnitude $\Delta\Omega/\Omega_0 = 3.1 \times 10^{-6}$ [22].

As well as the radio observations of the glitch in PSR B0833−45, our gravitational wave search makes use of Chandra X-ray telescope observations which determine the spin inclination ι and position angle ψ_G. The inclination is the angle between the pulsar's rotation axis and the line of sight to the Earth. The position angle is the angle between Celestial North and the spin axis, counterclockwise in the plane of the sky [23]. Finally, Hubble

PSR B0833−45		
Right ascension^a	α	$08^{\text{h}}35^{\text{m}}20.61149''$
Declination^a	δ	$-45°10'34.8751''$
Spin inclination^b	ι	$63.60^{+0.07}_{-0.05} \pm 1.3°$
Polarization Angle	ψ_G	$130.63^{+0.05}_{-0.07}$
Glitch epoch	T_{glitch}	MJD 53959.9392 ± 0.0002
		GPS 839457339 ± 17
		UTC 2006–08–12 22:31:22 ±17
Spin frequency	$\Omega_0/2\pi$	11.191455227602 ± 1.8 × 10^{-11} Hz
Frequency epoch		MJD 53945
Fractional glitch size^c	$\Delta\Omega/\Omega_0$	2.620×10^{-6}
Distance^d	$\mathcal{D}$	287^{+19}_{-17} pc

^{a}Taken from [25, 26]
^{b}Taken from [23]
^{c}Taken from [21]
^{d}Taken from [24]

TABLE I: Parameters of the Vela pulsar. The statistical and systematic errors in ι are listed as the first and second terms, respectively. The spin frequency and the glitch epoch were determined from the analysis described in Sec. II A. The error in the glitch epoch is an estimate of the 1-σ uncertainty. The glitch epoch quoted as MJD is defined in terms of barycentric dynamical time at the solar system barycenter. GPS and UTC times are terrestrial. The frequency epoch is the epoch at which the pre-glitch spin frequency was estimated.

Space Telescope observations of parallax indicate that Vela is a particularly nearby radio pulsar at a distance of just 287^{+19}_{-17} pc [24]. Table I gives a summary of parameters specific to the Vela pulsar and the August 2006 glitch. Further details and measurements can be found in the ATNF pulsar catalogue [25, 26].

B. LIGO data

At the time of the Vela glitch, LIGO was operating three laser interferometric detectors at two observatories in the United States. Two detectors were operating at the Hanford site, one with 4 km arms and another with 2 km arms. These are referred to as H1 and H2, respectively. A third detector, with 4 km arms, was operating at the Livingston site, referred to as L1. A full description of the configuration and status of the LIGO detectors during S5 can be found in [27]. There are no data from either the GEO 600 or Virgo gravitational wave detectors which cover the glitch epoch.

The data from the two Hanford detectors around the time of the pulsar glitch are of very high quality and completely contiguous for a time window centered on the glitch epoch lasting nearly five and a half hours. The Livingston detector was operating at the time of the glitch, but began to suffer from a degradation in data quality due to elevated seismic noise approximately thirty seconds later, and lost lock (the resonance condition of the Fabry-Perot arm cavities) less than three minutes after that. We have therefore chosen not to include L1

data in this analysis due to the instability of the detector during this period and the reduction in the amount of off-source data available (see Sec. IV). In GPS time, the glitch epoch is 839457339±17. There are 19586 seconds of data available from H1 and H2 in the period [839447317, 839466903) before H1 and H2 also begin to suffer from degradations in data quality. This entire contiguous segment is used in the analysis.

III. PULSAR GLITCHES & GRAVITATIONAL RADIATION

The physical mechanism behind pulsar glitches is not known. It is not even known if all glitches are caused by the same mechanism. Currently most theories fall into two classes: crust fracture ("star-quakes") and superfluid-crust interactions. These produce different estimates of the maximum energy and gravitational-wave strain to be expected.

The magnitudes of glitches in the Vela pulsar and the frequency with which they occur are indicative of being driven by the interaction of an internal superfluid with the solid crust of the neutron star [28]. For these superfluid-driven glitches, there may be a series of incoherent, band-limited bursts of gravitational waves due to an avalanche of vortex rearrangements [29]. This signal is predicted to occur during the rise-time of the glitch (≤ 40 seconds before the observed jump in frequency). A possible consequence of this vortex avalanche is the excitation of one or more of the families of global oscillations in the neutron star. These families are divided according

to their respective restoring forces (e.g., the fundamental (f) modes, pressure (p) modes, buoyancy (g) modes and space-time (w) modes) [30]. These oscillations will be at least partially damped by gravitational wave emission on timescales of milliseconds to seconds, leading to a characteristic gravitational wave signal in the form of a decaying sinusoid. There may also be a continuous periodic signal near the spin frequency of the star due to non-axisymmetric Ekman flow [31]. This emission dies away on the same time-scale as the post-glitch recovery of the pulsar spin frequency (~ 14 days).

Alternatively, the glitch may have been caused by a star-quake due to a spin-down induced relaxation of ellipticity [32], although the size and rate of the glitches mean that this cannot explain all of them [33]. In this case, it seems likely that oscillation modes will also be excited. The amount of excitation of the various mode families is not clear and will depend on the internal dynamics of the star during the quake.

Due to the gravitational-wave damping rates of the various mode families, it is reasonable to assume that the bulk of gravitational wave emission associated with oscillatory motion is generated by mass quadrupole (i.e. spherical harmonic index $l = 2$) f-mode oscillations. Furthermore, we make the simplifying assumption that a single harmonic dominates, so that the gravitational wave emission from the f-mode oscillations can be characterized entirely by the harmonic indices $l = 2$ and one of the $2l + 1$ values of m. This assumption and its astrophysical interpretation are discussed further in Sec. VII. The plus (+) and cross (×) polarizations for each spherical harmonic mode in this model are:

$$h_+^{2m}(t) = \begin{cases} h_{2m}\mathcal{A}_+^{2m}\sin[2\pi\nu_0(t-t_0)+\delta_0]e^{-(t-t_0)/\tau_0} \text{ for } t \geq t_0, \\ 0 \text{ otherwise.} \end{cases} \tag{3a}$$

$$h_\times^{2m}(t) = \begin{cases} h_{2m}\mathcal{A}_\times^{2m}\cos[2\pi\nu_0(t-t_0)+\delta_0]e^{-(t-t_0)/\tau_0} \text{ for } t \geq t_0, \\ 0 \text{ otherwise.} \end{cases} \tag{3b}$$

We refer to this decaying sinusoidal signal as a *ring-down* with frequency ν_0, damping time τ_0 and phase δ_0. The amplitude h_{2m} is the *peak intrinsic* gravitational wave strain emitted by any one of the various $l = 2, m = -2, \ldots, 2$ modes. The amplitude terms $\mathcal{A}_{+,\times}^{2m}$ encode the angular dependence of the gravitational wave emission around the star for the mth harmonic and depend on the line-of-sight inclination angle ι. Their explicit dependencies can be found in table II and are calculated from tensor spherical harmonics as in [34].

The f-mode frequency and damping time are sensitive to the equation of state of the neutron star, which is

Spherical Harmonic Indices	$\mathcal{A}_+^{2m}$	$\mathcal{A}_\times^{2m}$
$l = 2, \ m = 0$	$\sin^2\iota$	0
$l = 2, \ m = \pm 1$	$\sin 2\iota$	$2\sin\iota$
$l = 2, \ m = \pm 2$	$1 + \cos^2\iota$	$2\cos\iota$

TABLE II: The line-of-sight inclination angle ι dependencies of the expected polarizations in equations 3a and 3b for each set of spherical harmonic indices (l, m).

not known. Calculations of the frequency and damping time of the fundamental quadrupole mode for various

models of the equation of state, such as those in [35, 36], indicate that the frequency lies in the range $1 \lesssim \nu_0 \lesssim 3\,\mathrm{kHz}$ and the damping time lies in the range $0.05 \lesssim \tau_0 \lesssim 0.5\,\mathrm{seconds}$.

If we assume that a change in rotational angular frequency of size $\Delta\Omega$ is caused by a change in the moment of inertia, corresponding to a star-quake, it can be shown that the resulting change in rotational energy is given by $\Delta E = \frac{1}{2} I_* \Omega \Delta\Omega$, where I_* is the stellar moment of inertia and we assume conservation of angular momentum. Inserting fiducial values for the moment of inertia [37], rotational velocity and pulsar glitch magnitude we see that the characteristic energy associated with pulsar glitches driven by seismic activity is

$$\begin{aligned}
\Delta E_{\mathrm{quake}} \ \approx \ & 10^{42}\,\mathrm{erg} \ \left(\frac{I_*}{10^{38}\,\mathrm{kg\ m^2}}\right) \\
& \times \ \left(\frac{\Omega}{20\pi\,\mathrm{rad\ s^{-1}}}\right)^2 \left(\frac{\Delta\Omega/\Omega}{10^{-6}}\right),
\end{aligned} \qquad (4)$$

where we have used the spin-frequency of Vela and a glitch magnitude of $\Delta\Omega/\Omega = 10^{-6}$, typical of those in Vela. This is then the maximum energy that could be radiated in gravitational waves.

For superfluid-driven glitches, an alternative approach to computing the characteristic energy is to directly compute the change in gravitational potential energy resulting from the net loss of rotational kinetic energy in the context of a two-stream instability model [28]. In this picture, there exists a critical difference in the rotational angular frequency between a differentially rotating crust and superfluid interior. Beyond this critical *lag* frequency Ω_{lag}, the superfluid interior suddenly and dramatically couples to the solid crust. During the glitch, a fraction of the excess angular momentum in the superfluid is imparted to the crust so that the superfluid spins down while the crust spins up. It can then be shown that the change in the rotational energy is, to leading order, $\Delta E \approx -I_c \Omega^2 \left(\Delta\Omega/\Omega\right)\left(\Omega_{\mathrm{lag}}/\Omega\right)$, where I_c is the moment of inertia of the solid crust only. Inserting fiducial values, we find:

$$\begin{aligned}
\Delta E_{\mathrm{vortex}} \ \approx \ & 10^{38}\,\mathrm{erg} \ \left(\frac{I_c}{10^{37}\,\mathrm{kg\ m^2}}\right)\left(\frac{\Omega}{20\pi\,\mathrm{rad\ s^{-1}}}\right)^2 \\
& \times \ \left(\frac{\Delta\Omega/\Omega}{10^{-6}}\right)\left(\frac{\Omega_{\mathrm{lag}}/\Omega}{5\times10^{-4}}\right),
\end{aligned} \qquad (5)$$

where we have assumed $\Omega_{\mathrm{lag}} \sim 5 \times 10^{-4}\Omega$ [38] and we have assumed that the moment of inertia of the crust is about 10% of the total stellar moment of inertia.

An estimate of the intrinsic peak amplitude of gravitational waves emitted in the form of ring-downs as described by Eq. (3a) and Eq. (3b) can be found by integrating the luminosity of that signal over time and solid angle. Assuming that all of the rotational energy released by the glitch goes into exciting a single spherical harmonic and that the oscillations are completely damped by gravitational wave emission, we find that the expected peak amplitude of a ring-down signal is

$$\begin{aligned}
h_{2m} \ \approx \ & 10^{-23} \ \left(\frac{E_{2m}}{10^{42}\,\mathrm{erg}}\right)^{\frac{1}{2}} \left(\frac{2\,\mathrm{kHz}}{\nu_0}\right) \\
& \times \ \left(\frac{200\,\mathrm{ms}}{\tau_0}\right)^{\frac{1}{2}} \left(\frac{1\,\mathrm{kpc}}{\mathcal{D}}\right).
\end{aligned} \qquad (6)$$

IV. BAYESIAN MODEL SELECTION ALGORITHM

This search updates and deploys the model selection algorithm previously described in [39]. Bayesian model selection is performed by evaluating the ratio of the posterior probabilities between two competing models describing the data. Following the work in [39, 40] and [41], let us suppose our models represent some data D which contains a gravitational wave signal, called the *detection model*, denoted M_+, and data which does not contain a gravitational wave signal, called the *null-detection model*, M_-. Writing out the ratio of the posterior probabilities of each model, we see that

$$\begin{aligned}
\mathcal{O}_{(+,-)} \ = \ & \frac{\mathrm{P}(M_+|D)}{\mathrm{P}(M_-|D)} & (7a) \\
= \ & \frac{\mathrm{P}(M_+)}{\mathrm{P}(M_-)}\frac{\mathrm{P}(D|M_+)}{\mathrm{P}(D|M_-)}, & (7b)
\end{aligned}$$

The first term is commonly referred to as the *prior odds* and indicates the ratio of belief one has in the competing models prior to performing the experiment. Since it can be difficult to estimate, it is common to set this equal to unity. The second term, the *Bayes factor*, is the ratio of the marginal likelihoods or *evidences* for the data, given each model. For a model M_i described by a set of parameters $\vec{\mu}$, the evidence is computed from

$$\mathrm{P}(D|M_i) = \int_{\mu} p(\vec{\mu}|M_i)p(D|\vec{\mu}, M_i)\,\mathrm{d}\vec{\mu}, \qquad (8)$$

where $p(\vec{\mu}|M_i)$ is the prior probability density distribution on the parameters $\vec{\mu}$ and $p(D|\vec{\mu}, M_i)$ is the likelihood of obtaining the data D, given parameter values $\vec{\mu}$. The details of the models M_+ and M_- as used in this analysis are given in Sec. IV A.

The data analysis procedure is shown schematically in Fig. 1. Gravitational wave detector time series data centered on the pulsar glitch epoch and spanning the uncertainty in the epoch is obtained. This constitutes the *on-source* data and has duration T_{on} seconds. We also obtain a longer segment of time series data from before and after the on-source period. This is termed *off-source* data and is used to estimate the distribution and behaviour of the detection statistic (in our case, the odds ratio $\mathcal{O}_{(+,-)}$). The off-source data has total duration T_{off} seconds. This off-source data is then further divided into $N_{\mathrm{off}} = T_{\mathrm{off}}/T_{\mathrm{on}}$ trials, each of which will be used to compute one value of the odds ratio.
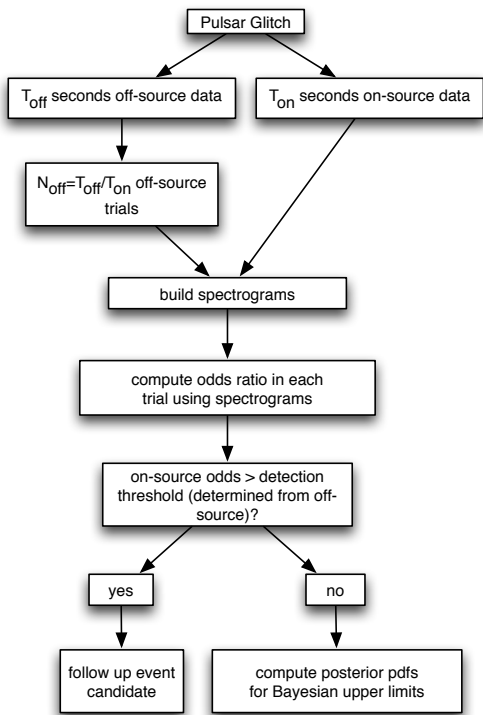
FIG. 1: A schematic view of the analysis pipeline. The odds ratio $\mathcal{O}_{(+,-)}$ is evaluated using on and off-source data near the pulsar timing glitch. If the odds ratio in the on-source data is greater than that expected from the distribution of odds ratios in in the off-source data, we have a candidate event for follow-up investigations. If there is no significant excess in $\mathcal{O}_{(+,-)}$ in the on-source data, we obtain upper limits on the gravitational wave amplitude and energy.

The data from each detector in the one on-source trial and each of the N_{off} off-source trials are then divided into short, overlapping time segments and a high-pass 12$^{\mathrm{th}}$ order Butterworth filter is applied with a knee frequency of 800 Hz. The power spectral density in that segment is then computed and we form a time-frequency map of power, or *spectrogram*, for each detector. The parameters used to construct the spectrograms are given in Table III. These spectrograms are then used as the data D_1 and D_2 from which we compute the odds ratio $\mathcal{O}_{(+,-)}$. Values of $\mathcal{O}_{(+,-)} \gg 1$ indicate a significant preference for the detection model.

The LIGO detector noise is, in general, non-stationary and can be found to contain instrumental or environmental transient signals which tend to mimic the gravitational wave signal we are looking for. To mitigate the risk of falsely claiming a gravitational wave detection, the off-source data is used to empirically determine the distribution of $\mathcal{O}_{(+,-)}$ when we do not expect a gravitational wave signal to be present. This allows us to estimate the statistical significance of any given value of

Parameter Space	
On-source data (GPS)	[839457279, 839457399)
Off-source data (GPS)	[839447317, 839457279)
	[839457399, 839466903)
LIGO antenna factors	$F_+ = -0.69,\ F_\times = -0.15$
Signal frequency (ν_0) range	$[1, 3]$ kHz
Decay time (τ_0) range	$[50, 500]$ ms
Amplitude ($\mathcal{A}_{\mathrm{eff}}$) range	$[10^{-22}, 10^{-19}]$
Spectrogram configuration	
Fourier segment length	2 seconds
Overlap	1.5 seconds
Frequency resolution	0.5 Hz
Data sampling frequency	16384 Hz

TABLE III: Parameters used in the gravitational wave data analysis. The antenna factors have been computed for the LIGO Hanford Observatory, the sky location and polarization angle for Vela, and the time of the glitch .

$\mathcal{O}_{(+,-)}$. We then compare the value of the odds ratio computed from the on-source data with this empirical distribution. If the significance of the on-source value of $\mathcal{O}_{(+,-)}$ is greater than the most significant off-source value then we have an interesting event candidate which merits further investigations such as a more robust estimate of its significance above the background level and verification with other data analysis pipelines. In this sense then, although the detection statistic itself, the odds ratio $\mathcal{O}_{(+,-)}$, is formed from Bayesian arguments, we choose a frequentist interpretation of its significance due to our inability to accurately model spurious instrumental noise features in the detector data. If no detection candidate is found, 90% confidence upper limits on the intrinsic gravitational wave strain amplitude h_{2m} and energy E_{2m} are found from their respective posterior probability density functions.

A. Signal model and computing the evidence for gravitational wave detection

Recall that we consider the detection and upper limits of each spherical harmonic mode (indexed by $l = 2,\ m$) separately. The response of an interferometric gravitational wave detector to an impinging gravitational wave is such that the time-domain signal in the detector output can be written

$$s^{2m}(t) = F_+(\boldsymbol{\Theta}, \psi_G)h_+^{2m}(t) + F_\times(\boldsymbol{\Theta}, \psi_G)h_\times^{2m}(t), \quad (9)$$

where $h_{+,\times}^{2m}$ are given by Eqs. (3a) and (3b). The terms $F_{+,\times}(\boldsymbol{\Theta}, \psi)$ are the detector response functions to the plus and cross polarizations of the gravitational waves, defined in [42]. These are functions of the sky location of the source $\boldsymbol{\Theta} = \{\alpha, \delta\}$, and the gravitational wave polarization angle ψ_G. We take the polarization angle to be equal to the position angle defined in [43]. For a single detector location and short-duration signal, where the antenna factors $F_{+,\times}$ are fixed, we are free to adopt a

simplified signal model and absorb all of the orientation factors ($F_{+,\times}$ and $\mathcal{A}_{+,\times}^{2m}$) into a single effective amplitude term $\mathcal{A}_{\text{eff}}$. Our time-domain signal model is finally

$$s(t) = \begin{cases} \mathcal{A}_{\text{eff}} \sin\left[2\pi\nu_0(t-t_0) + \delta_0'\right] e^{-(t-t_0)/\tau_0} & \text{for } t_0 \geq 0, \\ 0 & \text{otherwise,} \end{cases}$$

(10)

where the phase term δ_0' is now primed since it has been affected by the combination of the two signal polarizations into a single sinusoidal component. Note, however, that this analysis uses the power spectral density of the data and is insensitive to the signal phase.

We can then use the effective amplitude, the known inclination dependence encoded in the $\mathcal{A}_+$ and $\mathcal{A}_\times$ terms for the individual spherical harmonics, and the detector antenna factors F_+ and $F_\times$ to convert the effective amplitude $\mathcal{A}_{\text{eff}}$ to the intrinsic gravitational wave strain amplitude of the mth mode, h_{2m}:

$$h_{2m} = \frac{\mathcal{A}_{\text{eff}}}{\left[\left(F_+\mathcal{A}_+^{2m}\right)^2 + \left(F_\times\mathcal{A}_\times^{2m}\right)^2\right]^{\frac{1}{2}}},$$

(11)

which we note is insensitive to the sign of m. Upper limits on gravitational wave amplitude and energy are later presented for each value of $|m|$.

The likelihood function, which describes the probability of observing the power $\tilde{d}_{ij}$ in the (i^{th}, j^{th}) spectrogram pixel (time, frequency) given an expected signal power $\tilde{s}_{ij}(\vec{\mu})$, is a non-central χ^2 distribution with two degrees of freedom and a non-centrality parameter given by the expected contribution to the power from the model whose likelihood we are evaluating. For the case where a gravitational wave signal parameterized by $\vec{\mu}$ contributes power $\tilde{s}_{ij}(\vec{\mu})$, the joint likelihood for the entire spectrogram is

$$\begin{aligned} p(D|\vec{\mu}, M_+) = \prod_{i=1}^{N_{\text{T}}} \prod_{j=1}^{N_{\text{F}}} & \left\{ \frac{1}{2\sigma_j^2} \exp\left[-\frac{\tilde{d}_{ij} + \tilde{s}_{ij}(\vec{\mu})}{2\sigma_j^2}\right] \right. \\ & \left. \times \; I_0\left[\frac{1}{\sigma_j^2}\sqrt{\tilde{d}_{ij}\tilde{s}_{ij}(\vec{\mu})}\right] \right\}, \end{aligned}$$

(12)

where there are N_T total time bins in the spectrogram, N_F frequency bins and σ_j^2 is the variance of the noise power in the jth frequency bin. I_0 is the zeroth order modified Bessel function. The noise power variance σ_j^2 is estimated from the median noise power across time bins at that frequency using the data segment which is being analyzed. This method of estimating the noise is robust against bursts of power shorter than the length of the on-source data and avoids the potential contamination of the estimate of σ_j^2 from both instrumental noise artifacts and gravitational wave signals.

The prior probability distributions on the ring-down frequency ν_0 and damping time τ_0 are guided by the eigenmode calculations in [35] and [36]. The frequency prior is taken to be uniform between 1 and 3 kHz and the

damping time prior uniform between 50 and 500 ms. The glitch epoch for the search described here is found to have a 1-σ uncertainty of 17 seconds. We adopt a conservative flat prior range on the start time of the signal t_0 with a total width of 120 seconds, corresponding to over 3-σ on either side of the glitch epoch. In the detection stage of the analysis, the prior on the effective amplitude is chosen such that the probability density function is uniform across the logarithm of the effective amplitude:

$$p(\mathcal{A}_{\text{eff}}|M_+) = \frac{1}{\ln(\mathcal{A}_{\text{eff}}^{\text{upp}}/\mathcal{A}_{\text{eff}}^{\text{low}})\mathcal{A}_{\text{eff}}}.$$

(13)

This prior probability distribution is truncated at small ($\mathcal{A}^{\text{low}} = 10^{-22}$) and large ($\mathcal{A}^{\text{upp}} = 10^{-19}$) values to ensure that it is correctly normalized. The lower truncation is chosen to be much smaller than the effective amplitude produced by any detectable signal. That is, gravitational wave signals with effective amplitudes this small are indistinguishable from detector noise and we do not benefit from extending this lower limit. Similarly, the upper truncation is chosen to be well above the effective amplitude of easily detectable signals. However, when we come to form the posteriors on the amplitude and energy of gravitational waves we instead adopt a uniform prior on the effective amplitude on the range $[0, \infty)$, similar to the priors placed on frequency and decay time.

The reason for using these different priors in the different stages of the analysis is that, in the first stage, we wish to weight lower amplitude signals in keeping with astrophysical expectations and reduce the chance of falsely identifying a loud instrumental transient as a gravitational wave detection candidate. By the second stage, however, if we have already decided that there is no detection candidate, we aim to set conservative upper limits on gravitational wave amplitude and energy without introducing any additional bias towards low amplitudes. We find that the logarithmically uniform amplitude prior lowers (strengthens) the posterior amplitude upper limit from the uniform-amplitude case by as much as 50%. The linearly uniform amplitude prior is, therefore, more appropriate for the construction of conservative upper limits.

The search described in this work uses data D_1 and D_2 from two detectors. For the signal model, the data from each detector are combined by multiplying the likelihood of D_1 with the likelihood of D_2 between the detectors:

$$p(D|\vec{\mu}, M_+) = p(D_1|\vec{\mu}, M_+)p(D_2|\vec{\mu}, M_+). \quad (14)$$

Notice that this expression assumes that the data streams are uncorrelated. At the frequencies of interest to this search (i.e. 1–3 kHz), the dominant source of noise is photon shot noise which is not be correlated between detectors. Studies in [44] support this assumption. In addition, the frequentist interpretation of the odds ratios obtained from off-source trials provides an additional level of robustness against common correlated instrumental transient artifacts.

B. Computing the evidence against gravitational wave detection

We consider two possibilities which comprise the null-detection model: (i) Gaussian noise (model N) and (ii) an instrumental transient which is uncorrelated between detectors (model T). For the noise model, there is no contribution from any excess power due to gravitational waves or instrumental transients. The likelihood function for the full spectrogram is then given by the central χ^2 distribution with two degrees of freedom:

$$p(D|N) = \prod_{i=1}^{N_{\mathrm{T}}} \prod_{j=1}^{N_{\mathrm{F}}} \frac{1}{2\sigma_j^2} e^{-\bar{d}_{ij}/2\sigma_j^2}. \qquad (15)$$

A simple comparison between the signal model and χ^2 distributed noise is insufficient to discriminate real signals from instrumental transients due simply to the fact that *any* excess power tends to resemble the signal model more closely than the noise model. Following [45], we consider an alternative scenario for null-detection in which there is a transient signal of environmental or instrumental origin in the data. This artifact can mimic the gravitational wave ring-down signal we expect from the pulsar glitch. However, it may be present only in a single detector, or there may be temporally coincident instrumental transients with signal parameters inconsistent between detectors. In this case, the data D_1 and D_2 are independent, so the evidence for model T is simply the product of the evidences in each data stream,

$$\mathrm{P}(D|T) = \mathrm{P}(D_1|T)\mathrm{P}(D_2|T). \qquad (16)$$

The individual evidences are computed according to

$$\mathrm{P}(D_i|T) = \int_{\vec{\mu}} p(\vec{\mu}|T)p(D_i|\vec{\mu},T) \, \mathrm{d}\vec{\mu}. \qquad (17)$$

C. Detection statistic & upper limits

The total evidence for the null-detection model is the sum of the evidence for the instrumental transient model T and the noise-only model N and we are left with the following expression for $\mathcal{O}_{(+,-)}$, our detection statistic:

$$\mathcal{O}_{(+,-)} = \frac{\mathrm{P}(D|M_+)}{\mathrm{P}(D|T) + \mathrm{P}(D|N)}. \qquad (18)$$

Gravitational wave signals are correlated between detectors and, therefore, lead to higher evidence for the detection model M_+ than the transient model T. The transient model is also penalized relative to the signal model by virtue of the fact that the transient model has twice as many parameters over which it is marginalized. This yields a lower transient model evidence since it has been weighted down by twice the number of prior probability distributions. More importantly, instrumental transients

are generally uncorrelated between detectors. If a transient is only present in data stream D_1, for example, the likelihood from data D_2 will be very small. Multiplying these likelihoods inside the evidence integral for the detection model leads to nearly zero overall evidence for that model. The transient model T, by contrast, does not suffer this penalty so greatly since evidence may still be accumulated from other regions of parameter space before the separate evidence integrals are multiplied.

In the absence of a detection candidate, we compute the marginal posterior probability distribution on the effective amplitude $\mathcal{A}_{\mathrm{eff}}$, directly from the data using the likelihood function in equation 12 and the prior distributions discussed in the preceeding section. This posterior is then transformed into three separate posteriors for each value of $|m|$, according to Eq. (11). These are used to obtain Bayesian 90% upper limits on the intrinsic strain amplitudes, h_{2m}, by solving the following integral,

$$0.9 = \int_0^{h_{2m}^{90\%}} p(h_{2m}|D, M_+) \, \mathrm{d}h_{2m}. \qquad (19)$$

As described in Sec. III, we can use the expressions for the gravitational wave polarizations in Eqs. (3a) and (3b), to find the energy emitted by gravitational waves of different spherical harmonic modes by integrating the gravitational wave luminosity over solid angle and time. The resulting expressions for the energy from each harmonic all scale with the signal parameters $\{h_{2m},\ \nu_0,\ \tau_0\}$ and distance to the source $\mathcal{D}$ as,

$$E_{2m} \sim (h_{2m}\nu_0\mathcal{D})^2 \tau_0. \qquad (20)$$

The precise expression for each harmonic includes a different numerical factor, determined by integration of the $\mathcal{A}_{+,\times}^{2m}$ terms over solid angle. The relationships between the energies E_{2m} and our signal parameters allows us to form the marginal posterior probability density for the energy from the mth mode. These energy posteriors can then be used to find the energy upper limit by the same method as described above for the gravitational wave amplitude.

V. RESULTS

As stated in Sec. II B, we have a total of 19586 seconds of completely contiguous H1 and H2 data for use in the analysis. Our on-source region is 120 seconds centered on GPS time 839457339. This gives us 9962 seconds of off-source data prior to and 9504 seconds of off-source data following the on-source region. We assume that the noise characteristics of all of the off-source data remain constant and are representative of the on-source. We then split the off-source data into segments of 120 seconds to match the on-source region. We obtain a maximum of 161 trials which can be used to estimate the distribution of the odds ratio $\ln \mathcal{O}_{(+,-)}$ in the H1, H2 data. Figure 2
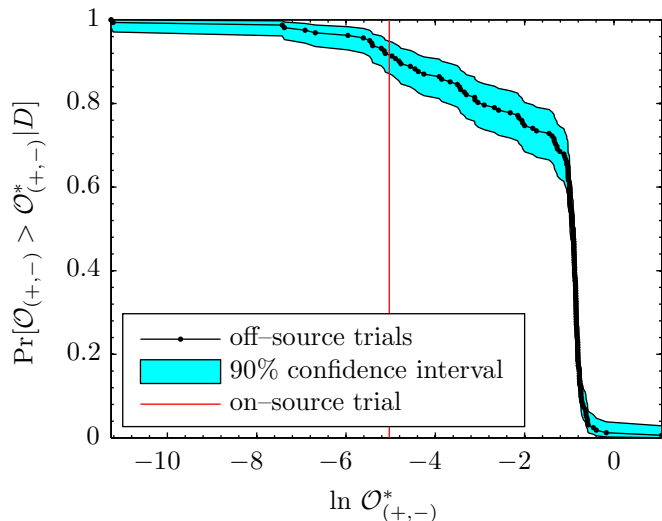
FIG. 2: The cumulative probability distribution function (CDF) for the off-source value of $\ln\mathcal{O}_{(+,-)}$. $\ln\mathcal{O}^*_{(+,-)}$ indicates the observed value. The shaded region shows the 90% confidence interval on the estimate of the CDF. The vertical line (red in the on-line version) indicates the value of $\ln\mathcal{O}_{(+,-)} = -5.03$ obtained from the on-source data segment. The probability of obtaining this value or greater from background alone is 0.92, where the red line intersects the black curve. The most significant off-source trial has $\ln\mathcal{O}_{(+,-)} = 1.07$ and the least significant has $\ln\mathcal{O}_{(+,-)} = -11.26$.

shows the cumulative distribution of $\ln\mathcal{O}_{(+,-)}$ in the off-source data. The largest value of the log odds found in the 161 off-source trials is $\ln\mathcal{O}_{(+,-)} = 1.07$. The minimum value is $\ln\mathcal{O}_{(+,-)} = -11.26$. Such a low value of the odds ratio indicates that there is strong evidence in favour of the null-detection model and that the data used for some this off-source trial contains one or more instrumental transients inconsistent with gravitational wave signals. We set a threshold equal to the loudest off-source value, above which we consider the on-source value to be significant enough to merit further investigation. The loudest off-source value of $\ln\mathcal{O}_{(+,-)} = 1.07$ corresponds to a false alarm probability of $1/161$. The odds of the detection model versus the null-detection model in the on-source data is $\ln\mathcal{O}_{(+,-)} = -5.03$, shown as the vertical line (red in the on-line version) in Fig. 2. Using the results from the off-source trials, we estimate that the probability of obtaining a value of $\mathcal{O}_{(+,-)}$ greater than the on-source value from background alone is 0.92. We therefore find no evidence in favour of gravitational wave emission in the form of a ring-down associated with this pulsar glitch.

The marginal posterior probability distributions and 90% confidence upper limits on the peak intrinsic amplitude h_{2m} and the total gravitational wave energy E_{2m} for each value of $|m|$ are shown in Figs. 3 and 4. The numerical values of the upper limits on amplitude and energy for different values of $|m|$ can be found in table IV.
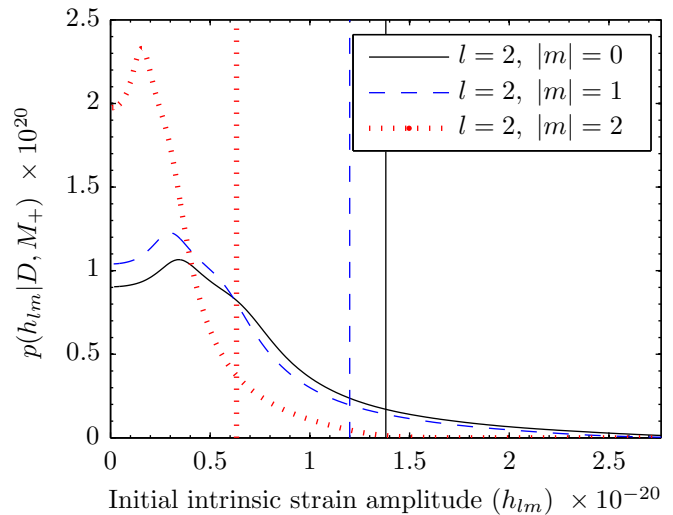

FIG. 3: The posterior probability density distributions and upper limits on the intrinsic peak amplitude of ring-downs, assuming only a single harmonic (i.e. value of $|m|$) is excited. The upper limits for each harmonic are shown as the vertical lines in the figure. The numerical values of the 90% confidence upper limits can be found in table IV. The $l = 2$, $|m| = 0$ posterior is shown as the solid (black) line, the dashed curve (blue in the on-line version) shows the $l = 2$, $|m| = 1$ posterior and the $l = 2$, $|m| = 2$ posterior is shown as the dotted curve (red in the on-line version).

Spherical Harmonic Indices	$h_{2m}^{90\%}$	$E_{2m}^{90\%}$ (erg)
$l = 2, \ m = 0$	1.4×10^{-20}	5.0×10^{44}
$l = 2, \ m = \pm 1$	1.2×10^{-20}	1.3×10^{45}
$l = 2, \ m = \pm 2$	6.3×10^{-21}	6.3×10^{44}

TABLE IV: The Bayesian 90% confidence upper limits on the intrinsic strain amplitude and energy associated with each spherical harmonic mode of oscillation.

We find that the different limits all lie within a factor of ~ 2 of one another. Note that these upper limits assume the signal model M_+ is correct and, unlike the detection statistic $\mathcal{O}_{(+,-)}$, do not directly account for instrumental transients.

During S5, the uncertainty in the magnitude of the detector response function in the frequency band of interest was $\sim 15\%$ in H1 and $\sim 11\%$ in H2 [46] leading to uncertainties in the amplitude and energy upper limits of $\sim 15\%$ and $\sim 30\%$, respectively. Note that H1 is the more sensitive detector and its calibration error dominates the analysis.

VI. PIPELINE VALIDATION

The analysis pipeline is validated and its performance is characterized by performing *software injections* whereby a population of simulated signals with param-
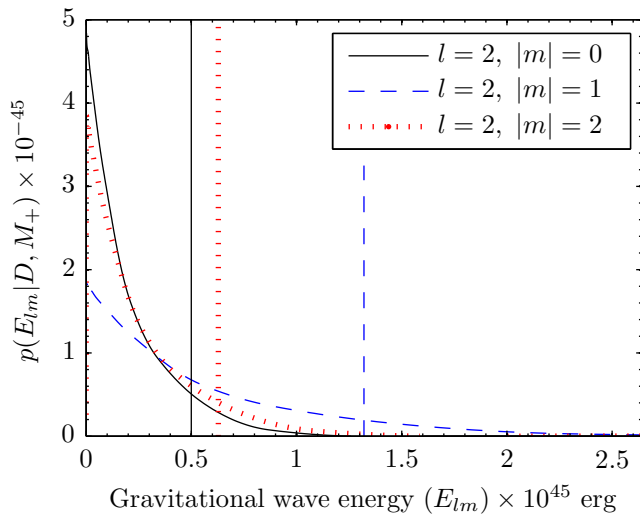
FIG. 4: The posterior probability density distributions and upper limits on the total gravitational wave energy in the form of ring-downs, assuming only a single harmonic (i.e. value of $|m|$) is excited. The upper limits for each harmonic are shown as the vertical lines in the figure. The numerical values of the 90% confidence upper limits can be found in table IV. The $l = 2$, $|m| = 0$ posterior is shown as the solid black line, the dashed curve (blue in the on-line version) shows the $l = 2$, $|m| = 1$ posterior and the $l = 2$, $|m| = 2$ posterior is shown as the dotted curve (red in the on-line version).
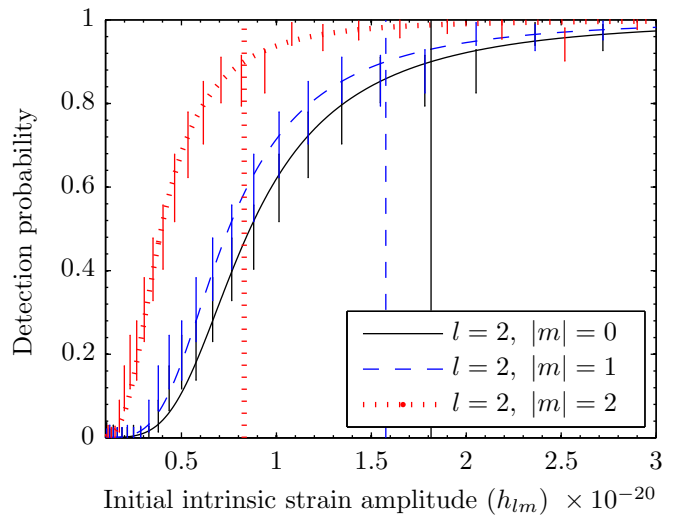

FIG. 5: Detection probabilities for software injections of ring-downs described by Eq. (10) and with parameters drawn from the prior distributions used in the search and described in Sec. IV A. Efficiencies are computed by counting the number of detections in discrete bins in amplitude. The three different curves correspond to the different harmonics (values of $|m|$). The long vertical lines indicate the 90% detection efficiencies for the different harmonics, whose numerical values are given in the text. The shorter vertical bars indicate 90% binomial confidence intervals in the estimate of the detection probability in each amplitude bin. The color-coding and line-style convention is the same as that in Figs. 3 and 4: The $l = 2$, $|m| = 0$ efficiency curve is shown as the solid black line, the dashed curve (blue in the on-line version) shows the $l = 2$, $|m| = 1$ efficiency curve and the $l = 2$, $|m| = 2$ efficiency curve is shown as the dotted curve (red in the on-line version).

eters drawn from the prior distributions described in Sec. IV A are added to detector time-series data prior to running the search algorithm. We then count what fraction of the injection population is recovered by the pipeline at increasing signal strengths. This fraction is the probability that a signal of a given strength will produce a value of $\mathcal{O}_{(+,-)}$ larger than the largest off-source value, providing a detection candidate.

Figure 5 shows the detection probabilities at increasing values of initial intrinsic gravitational wave amplitude for each harmonic mode. A single population of injections was generated with amplitudes drawn from the logarithmically uniform prior on the effective amplitude $\mathcal{A}_{\mathrm{eff}}$, given by Eq. (13). Injection frequencies and damping times are drawn from the uniform priors on those parameters. Injection start times, on the other hand, are drawn uniformly from both on- and off-source times as a check to ensure that there is no bias in detection efficiency between the on- and off-source data. The three curves corresponding to the harmonic modes $|m| = 0, 1, 2$ are generated by scaling the effective amplitudes by the detector antenna factors and appropriate inclination terms for each mode. We characterize the sensitivity of the pipeline by the initial amplitude required to reach 90% detection probability. These 90% detection efficiency amplitudes are marked in Fig. 5. For $l = 2$, $|m| = 0$, the 90% efficiency amplitude is $h_{20} = 1.8 \times 10^{-20}$; $l = 2$, $|m| = 1$ has 90% detection efficiency at $h_{21} = 1.6 \times 10^{-20}$ and

$l = 2$ $|m| = 2$ has 90% detection efficiency at 8.3×10^{-21}. These are $\sim 30\%$ larger than the corresponding Bayesian 90% confidence upper limits shown in Fig. 3. This discrepancy is not unexpected: the Bayesian amplitude posterior and the frequentist efficiency curve ask entirely different questions of the data. We therefore present the efficiency curve purely as evidence that the analysis pipeline could have detected a putative gravitational wave signal, *if there was one present*. The Bayesian upper limits, on the other hand, represent the strength of a gravitational wave signal we believe could have been present, *given the on-source observations*.

VII. DISCUSSION

We have performed a search for gravitational wave emission associated with a timing glitch in PSR B0833−45, the Vela pulsar, during the fifth LIGO science run. This search targeted ring-down signals in the frequency range [1, 3] kHz, with damping times in the range [50, 500] ms. No gravitational wave detection can-

didate was found. We place Bayesian 90% confidence upper limits on the intrinsic peak gravitational wave amplitude and total gravitational wave energy emitted by each quadrupolar spherical harmonic mode, assuming that only a single mode dominates any neutron star oscillations associated with the glitch. The amplitude and energy upper limits for the different modes are reported in table IV. The upper limits for each value of $|m|$ agree with one another to within a factor of ~ 2. Investigations of the impact of calibration uncertainties under a variety of scenarios suggest that the uncertainties in these upper limits are no more than $\sim 15\%$ and $\sim 30\%$ in amplitude and energy, respectively.

Having presented upper limits on the gravitational wave emission for the different possible values of the index m, we may ask what the physical interest is in the different cases. In the absence of a definitive model of the glitch mechanism, it is not possible to say in advance which m value is likely to be dominant. However, the different symmetries corresponding to the different m values offers some insight into the possible glitch mechanism. The $|m| = 0$ case corresponds to the excitation of modes whose eigenfunctions are symmetric about the rotation axis. In the context of glitches, this would be rather natural, as glitches are thought to be caused either by the build-up of a rotational lag (as in the superfluid model) or by a build-up of elastic strain energy in response to a decreasing centrifugal force (the star-quake model); both of these are axisymmetric in nature. The $|m| = 1$ case might correspond to a glitch that begins at one point in the star before propagating outwards. The $|m| = 2$ case might correspond to a glitch that inherits the symmetry of the magnetic dipole field that is believed to power the bulk of the star's spindown and radio pulsar emission. Clearly, a gravitational wave observation indicating which value of m (if any) of these is dominant will provide a unique insight into the glitch mechanism.

It is natural to compare the upper limits presented here with other gravitational wave searches for f-mode ring-downs. The only other search for a single f-mode event [13] presents a best upper limit of $E_{\mathrm{GW}}^{90\%} = 2.4 \times 10^{48}$ erg on the energy emitted in gravitational waves via f-mode induced ring-down signals associated with a flare from SGR 1806−20 on UTC 2006–08–24 14:55:26. In that analysis, however, the upper limits assume isotropic gravitational wave emission. In addition, the nominal distance of SGR 1806−20 is 10 kpc. To compare our results with those in [13], we must rescale our upper limit on the effective amplitude $\mathcal{A}_{\mathrm{eff}}$ to a source distance of 10 kpc, assume isotropic gravitational wave emission and use the average antenna factor of $(F_+^2 + F_\times^2)^{1/2} = 0.3$. We then find our equivalent, isotropic energy upper limit to be 1.3×10^{48} erg, a factor of ~ 2 lower than that in [13]. This improvement is to be expected since the

analysis presented here assumes that the signal waveform is a decaying sinusoid. The analysis in [13], by contrast, does not rely on a particular waveform and is designed to search for bursts of excess power with durations and frequencies compatible with f-mode ring-down signals.

Following the arguments laid out in Sec. III, the characteristic energy of a pulsar glitch is believed to be of order 10^{38} or 10^{42} erg, depending on the mechanism. Our current energy upper limits are 2–3 orders of magnitude above (weaker than) the more optimistic theoretical limit. The next generation of gravitational wave observatories currently under construction, such as advanced LIGO [47] and advanced Virgo [48], is expected to have noise amplitude more than an order of magnitude lower than in the current LIGO detectors at f-mode frequencies. This corresponds to probing energies more than two orders of magnitude lower than is currently possible, comparable to the order 10^{42} erg of the most optimistic theoretical predictions. The detection of gravitational waves associated with a Vela glitch in the advanced interferometer era is therefore possible and would provide compelling observational evidence for the star-quake theory of pulsar glitches. According to current conceptual design [49], the planned Einstein Telescope would improve noise amplitude at f-mode frequencies another order of magnitude beyond advanced LIGO, thereby improving the Vela glitch energy sensitivity two orders of magnitude to of order 10^{40} erg.

Acknowledgments

[1] B. P. Abbott et al., Astrophys. J. **713**, 671 (2010).

[2] J. Abadie et al. (2010), arXiv:gr-qc/1005.4655.

[3] J. Abadie et al., Astrophys. J. **715**, 1453 (2010).
[4] K. S. Thorne and A. Campolattaro, Astrophys. J. **149**, 591 (1967).
[5] R. Price and K. S. Thorne, Astrophys. J. **155**, 163 (1969).
[6] K. S. Thorne, Astrophys. J. **158**, 1 (1969).
[7] K. S. Thorne, Astrophys. J. **158**, 997 (1969).
[8] A. Campolattaro and K. S. Thorne, Astrophys. J. **159**, 847 (1970).
[9] J. R. Ipser and K. S. Thorne, Astrophys. J. **181**, 181 (1973).
[10] K. D. Kokkotas and B. Schmidt, Living Reviews in Relativity **2** (1999), URL http://www.livingreviews.org/lrr-1999-2.
[11] M. Benacquista, D. M. Sedrakian, M. V. Hairapetyan, K. M. Shahabasyan, and A. A. Sadoyan, Ap. J. Lett. **596**, L223 (2003).
[12] J. A. de Freitas Pacheco, Astron. Astrophys. **336**, 397 (1998).
[13] B. P. Abbott et al., Phys. Rev. Lett. **101**, 211102 (2008).
[14] B. P. Abbott et al., Ap. J. Lett. **701**, L68 (2009).
[15] R. Oechslin and H. Janka, Phys. Rev. Lett. **99**, 121102 (2007).
[16] J. Middleditch, F. E. Marshall, Q. D. Wang, E. V. Gotthelf, and W. Zhang, Astrophys. J. **652**, 1531 (2006).
[17] P. W. Anderson and N. Itoh, Nature **256**, 25 (1975).
[18] S. Buchner and C. Flanagan, in *40 Years of Pulsars: Millisecond Pulsars, Magnetars and More* (2008), vol. 983 of *American Institute of Physics Conference Series*, pp. 145–147.
[19] S. L. Shemar and A. G. Lyne, Mon. Not. R. Astron. Soc. **282**, 677 (1996).
[20] G. B. Hobbs, R. T. Edwards, and R. N. Manchester, Mon. Not. R. Astron. Soc. **369**, 655 (2006).
[21] C. S. Flanagan and S. J. Buchner, Central Bureau Electronic Telegrams **595**, 1 (2006).
[22] R. G. Dodson, P. M. McCulloch, and D. R. Lewis, Ap. J. Lett. **564**, L85 (2002).
[23] C. Y. Ng and R. W. Romani, Astrophys. J. **673**, 411 (2008).
[24] R. Dodson, D. Legge, J. E. Reynolds, and P. M. McCulloch, Astrophys. J. **596**, 1137 (2003).
[25] *Australia Telescope National Facility Pulsar Catalogue* *http://www.atnf.csiro.au/research/pulsar/psrcat*.
[26] R. N. Manchester, G. B. Hobbs, A. Teoh, and M. Hobbs, Astron. J. **129**, 1993 (2005).
[27] B. P. Abbott et al., Rept. Prog. Phys. **72**, 076901 (2009).
[28] N. Andersson, G. L. Comer, and R. Prix, Mon. Not. R. Astron. Soc. **354**, 101 (2004).
[29] A. Melatos, C. Peralta, and J. S. B. Wyithe, Astrophys. J. **672**, 1103 (2008).
[30] T. Sidery, A. Passamonti, and N. Andersson, Mon. Not. R. Astron. Soc. **405**, 1061 (2010).
[31] C. A. van Eysden and A. Melatos, Class. Quantum Grav. **25**, 225020 (2008).
[32] M. Ruderman, Nature **223**, 597 (1969).
[33] G. Baym and D. Pines, Ann. Phys. (N.Y.) **66**, 816 (1971).
[34] K. S. Thorne, Reviews of Modern Physics **52**, 299 (1980).
[35] N. Andersson and K. D. Kokkotas, Mon. Not. R. Astron. Soc. **299**, 1059 (1998).
[36] O. Benhar, V. Ferrari, and L. Gualtieri (AIP Conf. Proc., 2005), vol. 751, pp. 211–213.
[37] J. M. Lattimer and M. Prakash, Astrophys. J. **550**, 426 (2001).
[38] A. G. Lyne, S. L. Shemar, and F. G. Smith, Mon. Not. R. Astron. Soc. **315**, 534 (2000).
[39] J. Clark, I. S. Heng, M. Pitkin, and G. Woan, Phys. Rev. D **76**, 043003 (2007).
[40] J. Veitch and A. Vecchio, Class. Quantum Grav. **25**, 184010 (2008).
[41] A. C. Searle, P. J. Sutton, M. Tinto, and G. Woan, Class. Quantum Grav. **25**, 114038 (2008).
[42] P. Jaranowski, A. Królak, and B. F. Schutz, Phys. Rev. D **58**, 063001 (1998).
[43] C. Y. Ng and R. W. Romani, Astrophys. J. **601**, 479 (2004).
[44] B. P. Abbott et al., Phys. Rev. **D80**, 102002 (2009).
[45] J. Veitch and A. Vecchio, Phys. Rev. D **81**, 062003 (2010).
[46] J. Abadie et al. (2010), arXiv:gr-qc/1007.3973.
[47] G. M. Harry et al., Class. Quantum Grav. **27**, 084006 (2010).
[48] http://wwwcascina.virgo.infn.it/advirgo/.
[49] M. Punturo et al., Classical and Quantum Gravity **27**, 084007 (2010).